Plasticity size effects in tension and compression of single crystals

Deshpande, VS; Needleman, A; Van der Giessen, E

Published in:
Journal of the Mechanics and Physics of Solids

DOI:
10.1016/j.jmps.2005.07.005

Publication date:
2005

Available online at www.sciencedirect.com
SCIENCE DIRECT®
Journal of the Mechanics and Physics of Solids
53 (2005) 2661–2691
JOURNAL OF THE MECHANICS AND PHYSICS OF SOLIDS
www.elsevier.com/locate/jmps

Plasticity size effects in tension and compression of single crystals

V.S. Deshpande[a,*], A. Needleman[b], E. Van der Giessen[c]

[a]*Department of Engineering, Cambridge University, Trumpington Street, Cambridge CB2 1PZ, UK*
[b]*Division of Engineering, Brown University, Providence, RI 02912, USA*
[c]*Materials Science Center, University of Groningen, Nyenborgh 4, 9747 AG Groningen, The Netherlands*

Received 24 February 2005; received in revised form 13 July 2005; accepted 15 July 2005

Abstract

The effect of size and loading conditions on the tension and compression stress–strain response of micron-sized planar crystals is investigated using discrete dislocation plasticity. The crystals are taken to have a single active slip system and both small-strain and finite-strain analyses are carried out. When rotation of the tensile axis is constrained, the build-up of geometrically necessary dislocations results in a weak size dependence but a strong Bauschinger effect. On the other hand, when rotation of the tensile axis is unconstrained, there is a strong size dependence, with the flow strength increasing with decreasing specimen size, and a negligible Bauschinger effect. Below a certain specimen size, the flow strength of the crystals is set by the nucleation strength of the initially present Frank–Read sources. The main features of the size dependence are the same for the small-strain and finite-strain analyses. However, the predicted hardening rates differ and the finite-strain analyses give rise to some tension–compression asymmetry.

Keywords: Dislocations; Size effects; Plasticity; Computer simulation

*Corresponding author. Tel.: +44 1223 332664; fax: +44 1223 332662.
E-mail address: vsd@eng.cam.ac.uk (V.S. Deshpande).

0022-5096/$ - see front matter © 2005 Elsevier Ltd. All rights reserved.
doi:10.1016/j.jmps.2005.07.005

1. Introduction

There is a considerable body of experimental evidence that plastic deformation in crystalline solids is size dependent at length scales of the order of tens of microns and smaller, (e.g. Ebeling and Ashby, 1966; De Guzman et al., 1993; Fleck et al., 1994; Ma and Clarke, 1995). One well-appreciated source of this size dependence is associated with plastic strain gradients and geometrically necessary dislocations. Size effects can arise at the micron scale even when the macroscopically applied deformation is uniform. Typically, this occurs when dislocation motion is constrained, as in a thin film on a substrate or due to grain boundaries or internal interfaces. Although an overall homogeneous deformation is possible, the constraint on dislocation motion induces a nonuniform deformation state. Often, but not always, this manifests itself in a hard boundary layer. In addition, self-organized dislocation structures of the type observed by Hughes and Hansen (1993) can develop and give rise to a size effect.

On the other hand, when plastic deformation is unconstrained and when the loading is compatible with an overall homogeneous deformation state, a size independent response is expected even at the micron scale. Therefore, it is somewhat surprising that a strong size effect is seen in the single crystal compression tests of Uchic et al. (2004), Greer et al. (2005) and Dimiduk et al. (2005). In these experiments, cylinders, with diameters from 0.5 to 40 μm and height to diameter ratios in the range 2:1 to 4:1, were machined from a bulk single crystal using a focused ion beam microscope (FIB) and subjected to uniaxial compression using a nanoindenter with a flat tip. While the Ni and Ni_3Al intermetallic crystals of Uchic et al. (2004) were oriented for single slip, Greer et al. (2005) employed gold single crystals mainly oriented in a symmetric double slip configuration. In these experiments, the flow strength of the smallest specimens was about an order of magnitude greater than that of the larger specimens but still substantially below the theoretical strength that would be expected to prevail for defect free whiskers. Size effects at a similar size scale are also seen in polycrystalline thin films, even when free standing, (e.g. Legros et al., 2000; Zupan et al., 2001; Haque and Saif, 2004; Xiang et al., 2004). Unlike in the experiments of Uchic et al. (2004), Greer et al. (2005) and Dimiduk et al. (2005), grain size effects are expected to play a significant role in these thin film experiments.

In order to shed further light on these size effects, we carry out analyses of planar single crystals subject to both tension and compression. Attention is confined to single slip, and plastic flow arises from the collective motion of discrete edge dislocations. They are represented as line singularities in an elastic solid, with the long-range interactions between dislocations and with free surfaces being directly accounted for. Drag during dislocation motion, interactions with obstacles, and dislocation nucleation and annihilation are incorporated through a set of constitutive rules. Two sets of boundary conditions are considered. In one case, the tensile axis is free to rotate while in the other case the rotation of the tensile axis is constrained. Because of the possible significant effect of lattice rotations, both small-strain and finite-strain calculations are carried out. For both sets of boundary

conditions, crystal sizes ranging from 0.25 to 8 μm are considered. Results are presented for the effect of size and loading conditions—constrained versus unconstrained tensile axis rotation and tension versus compression—on the stress–strain response.

2. Small-strain discrete dislocation formulation

The crystals are taken to be elastically isotropic with Young's modulus E and Poisson's ratio ν. Plane strain conditions are assumed with the x_1-x_2-plane, the plane of deformation and geometry changes neglected. The crystals have one slip system at an angle ϕ with the positive x_1 axis. The geometry and boundary conditions employed are described in Section 2.1.

Plastic deformation, when it occurs, is described by the nucleation and glide of discrete edge dislocations, represented as line singularities in an elastic medium, with Burgers vector b. Once dislocations nucleate, field quantities are computed using superposition. The singular ($\tilde{}$) field associated with the N dislocations is calculated analytically from the isotropic linear elastic infinite medium fields of the dislocations. The complete solution is obtained by adding an image ($\hat{}$) field that ensures that the boundary conditions are satisfied. Thus, the displacements, strains and stresses are expressed as

$$u_i = \hat{u}_i + \tilde{u}_i, \quad \varepsilon_{ij} = \hat{\varepsilon}_{ij} + \tilde{\varepsilon}_{ij}, \quad \sigma_{ij} = \hat{\sigma}_{ij} + \tilde{\sigma}_{ij}, \tag{1a}$$

respectively, where the ($\tilde{}$) field is the sum of the fields of the individual dislocations in their current positions, i.e.

$$\tilde{u}_i = \sum_{I=1}^{N} \tilde{u}_i^{(I)}, \quad \tilde{\sigma}_{ij} = \sum_{I=1}^{N} \tilde{\sigma}_{ij}^{(I)}, \quad \tilde{\varepsilon}_{ij} = \sum_{I=1}^{N} \tilde{\varepsilon}_{ij}^{(I)}. \tag{1b}$$

The image ($\hat{}$) field is obtained by solving a linear elastic boundary value problem with boundary conditions that change as the dislocation structure evolves (Van der Giessen and Needleman, 1995).

At the beginning of a calculation the crystal is stress- and dislocation-free. The long range interactions of the dislocations are accounted for through their elastic fields while constitutive rules are prescribed for short range interactions. New dislocation pairs are generated by simulating Frank–Read sources. In two dimensions, this is mimicked by discrete point sources randomly distributed on discrete slip planes which generate a dislocation dipole with their Burgers vectors aligned with the slip plane direction. This occurs when the magnitude of the Peach–Koehler force $f^{(I)}$ on source I exceeds a critical value $\tau_{\text{nuc}}b$ during a time period t_{nuc}. The sign of the dipole is determined by the sign of the resolved shear stress along the slip plane while the distance between the two dislocations at nucleation, L_{nuc}, is taken such that the attractive stress field that the dislocations exert on each other is equilibrated by a shear stress of magnitude τ_{nuc}. Annihilation of two opposite signed dislocations on a slip plane occurs when they are within a

material-dependent critical annihilation distance L_e. The magnitude of the glide velocity $V_{\text{gln}}^{(I)}$ along the slip direction of dislocation I is taken to be linearly related to the Peach–Koehler force $f^{(I)}$ through the drag relation

$$V_{\text{gln}}^{(I)} = \frac{1}{B} f^{(I)}, \tag{2}$$

where B is the drag coefficient. Obstacles to dislocation motion are modeled as points associated with a slip plane. Dislocations on the obstacle slip plane get pinned as they try to pass through that point. Obstacles release pinned dislocations when the Peach–Koehler force on the obstacle exceeds $\tau_{\text{obs}} b$.

2.1. Boundary conditions

The undeformed specimen is of dimension $2L \times W$ with the tensile axis aligned with the x_1 direction, see Fig. 1. Tension is imposed by prescribing

$$u_1 = U, \quad T_2 = 0 \quad \text{on } x_1 = 2L, \tag{3a}$$

and

$$u_1 = -U, \quad T_2 = 0 \quad \text{on } x_1 = 0, \tag{3b}$$

where $T_i = \sigma_{ij} n_j$ is the traction on the boundary with outward normal n_j. The lateral edges, on $x_2 = \pm W/2$, are traction free, i.e.

$$T_1 = T_2 = 0. \tag{4}$$

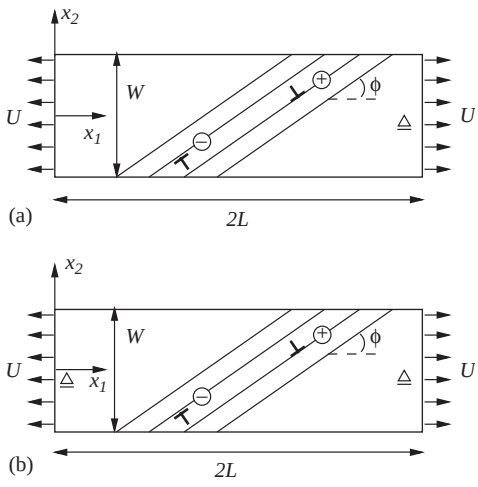

Fig. 1. Sketch of the single crystal specimen analyzed and the sign convention employed for the edge dislocations. Tensile axis rotation (a) unconstrained and (b) constrained boundary conditions.

A time step of $\Delta t = 0.5\,\text{ns}$ is needed to resolve the dislocation dynamics so a rather high loading rate $\dot{U}/L = 2000\,\text{s}^{-1}$ is used to obtain a strain of 0.01 in 10,000 time steps. With these common set of boundary conditions we explore the effect of the constraint imposed by the tensile grips by considering the following two additional constraints:

(i) *Unconstrained rotation of the tensile axis*: $u_2 = 0$ is imposed on one material point at $(2L - x_\varepsilon, 0)$, where $x_\varepsilon = 0.1L$. This prevents rigid body translation in the x_2 direction but does not restrict the rotation of the tensile axis of the specimen. Even though the rotation of the tensile axis of the specimen is unconstrained, the displacement boundary conditions, Eq. (3), prevent the rotation of the ends of the specimen. This condition is representative of the constraints in the compression tests of Uchic et al. (2004) and Greer et al. (2005).

(2) *Constrained rotation of the tensile axis*: $u_2 = 0$ is imposed on two material points: at $(2L - x_\varepsilon, 0)$ as above and at $(x_\varepsilon, 0)$. This simulates the constraint imposed by the grips which prevents the rotation of the line spanning $(x_\varepsilon, 0)$ to $(2L - x_\varepsilon, 0)$, referred to here as the tensile axis. This is representative of the constraints in the micro-sample tensile tests of Legros et al. (2000) and Haque and Saif (2004).

The applied stress σ is computed as

$$\sigma = -\frac{1}{W}\int_{-W/2}^{W/2} T_1(0, x_2)\,\mathrm{d}x_2, \tag{5}$$

to give the stress versus strain U/L response of the specimens.

2.2. Reference properties

In all calculations here, the specimen aspect ratio was fixed at $L/W = 1.5$ to match the aspect ratio in the experiments of Uchic et al. (2004) and the specimen sizes varied from $W = 0.25\,\mu\text{m}$ to $W = 8.0\,\mu\text{m}$. The crystals are taken to be elastically isotropic with Young's modulus $E = 70\,\text{GPa}$ and Poisson's ratio $\nu = 0.33$ and have slip planes at an angle $\phi = 45^\circ$ with the positive x_1 axis. The slip planes are spaced $100b$ apart, where $b = 0.25\,\text{nm}$ is the magnitude of the Burger's vector of the edge dislocations in the crystals. The slip planes are distributed over two-thirds of the specimen length such that none intersect the edges where displacements are prescribed (Fig. 1) in order to avoid numerical complications that would occur if dislocations were to attempt to exit the material through these edges. A reference material is considered which has Frank–Read sources randomly distributed on these slip planes with a density $\rho_{\text{src}} = 56\,\mu\text{m}^{-2}$. Each source is randomly assigned a nucleation strength, τ_{nuc}, from a Gaussian distribution with average $\bar{\tau}_{\text{nuc}} = 50\,\text{MPa}$ and standard deviation $\Delta\tau_{\text{nuc}} = 1.0\,\text{MPa}$. The nucleation time for the sources t_{nuc} is taken to be 10 ns. The drag coefficient for dislocation glide $B = 10^{-4}\,\text{Pa s}$, which is representative of Al (Kubin et al., 1992). Obstacles of strength $\tau_{\text{obs}} = 150\,\text{MPa}$ are randomly distributed with a density $\rho_{\text{obs}} = 56\,\mu\text{m}^{-2}$ while the material dependent

annihilation distance $L_e = 6b$. The sensitivity of the results to the values of some of these parameters is explored.

2.3. Details of the finite element mesh

Since the ($\tilde{}$) fields are given analytically, the finite element mesh needs to resolve the ($\hat{}$) fields, not the total fields. Thus, the element size is taken so as to resolve the ($\hat{}$) field gradients. Typically, for the uniaxial tension problem under consideration, wavelengths associated with the ($\hat{}$) fields scale with the specimen size and thus in all the small-strain calculations, a uniform finite element grid was employed comprising of 80×40 bilinear quadrilaterals. This corresponds to a maximum element size of 0.0094 and 0.3 μm for the $W = 0.25$ and 8.0 μm crystals, respectively. Mesh sensitivity studies were carried out on the $W = 2.0$ μm crystals, and revealed that decreasing the mesh size by a factor of two had little effect on the numerical results presented subsequently.

3. Small-strain numerical results

For both the calculations with rotation of the tensile axis constrained and unconstrained, the small-strain tensile and compressive responses of the crystals are identical. Thus, while the results discussed subsequently were calculated for tensile loading, they hold equally for compressive loading. Unless otherwise specified, all calculations pertain to the reference properties given in Section 2.2.

3.1. Tensile axis rotation unconstrained

The tensile stress, σ, versus strain, U/L, responses of three specimen sizes of the reference crystals are plotted in Fig. 2a. In all calculations in Fig. 2a, the first dislocation activity occurs at $\sigma \approx 95$ MPa. Since the Schmid factor for the slip system is $(\sin 2\phi)/2 = 0.5$, this value is consistent with the mean value of the source strength distribution being $\bar{\tau}_{\text{nuc}} = 50$ MPa. Subsequently, for the $W = 1.0$ and 4.0 μm specimens, there is a sharp drop in the stress followed by essentially an ideally plastic response. On the other hand, there is nearly no stress drop in the $W = 0.25$ μm specimen with large periodic fluctuations in the applied stress about a fixed mean value of the applied stress. The corresponding evolution of the dislocation density ρ_{dis} (number of dislocations per unit area in a central $2L/3 \times W$ region) is shown in Fig. 2b: ρ_{dis} increases with increasing U/L before leveling off at strain levels at which the applied stress remains approximately constant. While the curves of the evolution of ρ_{dis} with U/L are relatively smooth for the $W = 1.0$ and 4.0 μm specimens, periodic fluctuations in ρ_{dis} are seen for the $W = 0.25$ μm specimen. These periodic fluctuations are associated with the nucleation and exit of dislocations from the $x_2 = \pm W/2$ traction free boundaries and also correspond to the fluctuations in the σ versus U/L response of the $W = 0.25$ μm specimen in Fig. 2a. It is worth noting that in this specimen, the rate of dislocation nucleation is

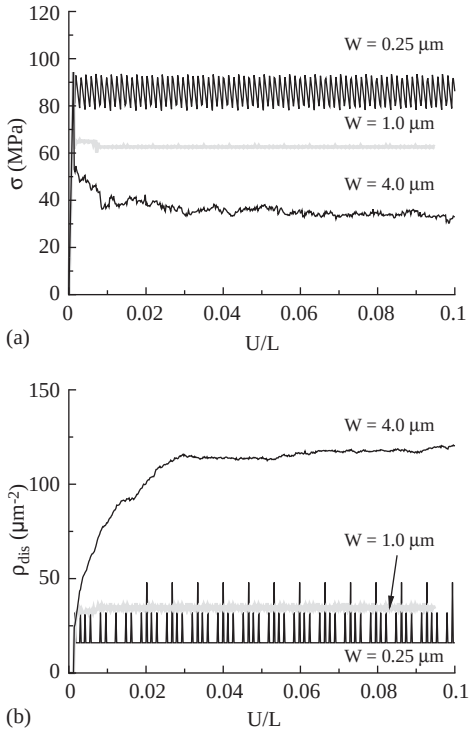

Fig. 2. Small-strain results for the tensile response (rotation of the tensile axis unconstrained) for three specimen sizes. (a) Nominal stress versus nominal tensile strain and (b) evolution of the dislocation density with nominal tensile strain.

approximately equal to the rate at which dislocations exit the specimen and thus at no stage are there more than three dislocations present in the $W = 0.25\,\mu m$ specimen.

The results in Fig. 2 show that both the flow strength and dislocation density are strongly dependent on the specimen size W. In order to quantify this size dependence, the flow strength σ_f (defined as the average stress between $0.04 \leqslant U/L \leqslant 0.05$) is plotted in Fig. 3a as a function of the specimen size W. The corresponding variation of the dislocation density ρ_f, also averaged over $0.04 \leqslant U/L \leqslant 0.05$, with specimen size W is included in Fig. 3b. The results indicate that the flow strength σ_f increases with decreasing W before leveling off at $W \approx 0.375\,\mu m$ while the dislocation density ρ_f increases with increasing W and starts to plateau at $W \approx 4.0\,\mu m$. In an attempt to quantify the statistical variations in these results, calculations for each specimen size were repeated with two additional spatial distributions of the sources and obstacles (all with the same overall source and obstacle densities $\rho_{nuc} = \rho_{obs} = 56\,\mu m^{-2}$). The predicted values of σ_f and ρ_f from these calculations are plotted in Fig. 3 and labeled realizations 1 to 3. For the large specimen sizes ($W = 4.0$ and $8.0\,\mu m$), σ_f values are nearly identical for the three

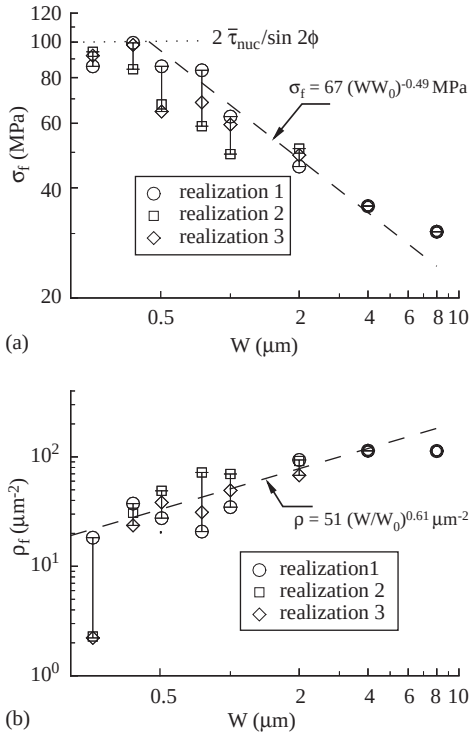

Fig. 3. (a) Flow strength σ_f and (b) average dislocation density ρ_f as a function of the specimen size W. Small-strain results (rotation of the tensile axis unconstrained) for three realizations of the reference case.

realizations as there about approximately 10^4 dislocations in these specimens. On the other hand, there is about a 10% variation in σ_f for the $W < 0.4\,\mu m$ specimens. In these specimens, there are typically 2–10 dislocations present at any stage of the deformation. Thus, for a sufficiently small specimen, σ_f is mainly governed by the nucleation stress τ_{nuc} and the variation in σ_f in the different realizations is a result of the Gaussian distribution in $\bar{\tau}_{nuc}$. Variations in the values of σ_f are greatest for the intermediate size specimens with σ_f showing a 25% variation between the three realizations for the $W = 0.75\,\mu m$ specimen. The strength of these specimens is governed by the structures formed by a relatively small number of dislocations and thus is sensitive to statistical variations.

A power-law relation of the form

$$\sigma_f = \alpha\left(\frac{W}{W_0}\right)^{-n}, \tag{6}$$

where $W_0 = 1\,\mu m$ is a reference size, fits the data in Fig. 3a well over the range $0.75\,\mu m \leqslant W \leqslant 4.0\,\mu m$ with the choices $\alpha = 67\,MPa$ and $n = 0.49$. Fig. 3a indicates that while the flow strength scales approximately as $\sigma_f \propto W^{-0.5}$ for intermediate

sizes, there exist lower and upper plateaus of the flow strength with the large specimens ($W = 8.0\,\mu m$) having a flow strength higher than that given by Eq. (6) while the small specimens ($W < 0.4\,\mu m$) have a flow strength less than that estimated from Eq. (6) (since the flow strength of the small specimens is governed by the nucleation stress of the sources, $\sigma_f \approx 2\bar{\tau}_{nuc}/\sin 2\phi$ for $W < 0.4\,\mu m$). We also fit a power-law relation of the form

$$\rho_f = \beta\left(\frac{W}{W_0}\right)^m, \tag{7}$$

to the dislocation density data in Fig. 3b for $0.75\,\mu m \leqslant W \leqslant 4.0\,\mu m$, with $\beta = 51\,\mu m^{-2}$ and $m = 0.61$. The fit reveals that ρ_f has begun to plateau by $W = 4.0\,\mu m$ with the value for $W = 8.0\,\mu m$ being lower than that expected from an extrapolation of Eq. (7).

Distributions of the stress σ_{11} in the $W = 0.5, 2.0$ and $4.0\,\mu m$ specimens at $U/L = 0.05$ are shown in Figs. 4a–c, respectively. The predicted dislocation structures at $U/L = 0.05$ are also included in Fig. 4. The stress distribution is nearly uniform in the $W = 0.25\,\mu m$ specimen with the stress concentrations associated with the individual dislocations clearly visible. This confirms that the flow strength is

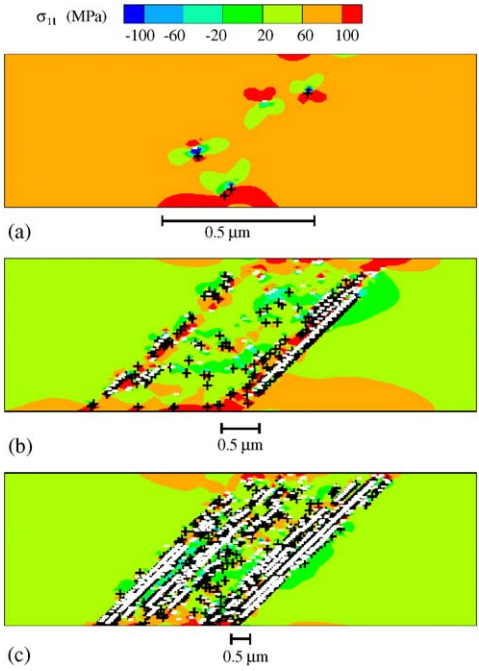

Fig. 4. Small-strain results (rotation of the tensile axis unconstrained) for the distribution of σ_{11} and the dislocation structure in the (a) $W = 0.5\,\mu m$, (b) $W = 2.0\,\mu m$ and (c) $W = 4.0\,\mu m$ specimens at an applied strain $U/L = 0.05$. The black "+" symbols denote dislocations with Burgers vector $+b$ and the white "−" symbols denote dislocations with Burgers vector $-b$ (see Fig. 1 for the sign convention).

governed by the strength $\bar{\tau}_{\text{nuc}}$ of the Frank–Read sources. The stress levels are lower in the $W = 1.0\,\mu\text{m}$ specimen with dislocations concentrated in two distinct slip bands. Furthermore, a dislocation-free boundary layer $\approx 0.5\,\mu\text{m}$ wide forms near the traction free $x_2 = \pm W/2$ surfaces. A similar boundary layer forms in the $W = 4.0\,\mu\text{m}$ specimen but occupies a much smaller area fraction of the $4.0\,\mu\text{m}$ specimen resulting in a more homogeneous stress distribution.

We proceed to investigate the size dependence of the energy stored in the dislocation structures in these single crystals. The elastic energy (per unit thickness) stored in a specimen of area A is given by

$$\Phi = \frac{1}{2}\int_A \sigma_{ij}\varepsilon_{ij}\,\mathrm{d}A, \tag{8}$$

which includes contributions from the applied loads and the energy associated with the dislocation structure. In calculating Φ, a region of radius $4b$ is excluded around each dislocation core. Numerical checks showed that decreasing the core radius to $2b$ had a negligible effect on Φ, although the order of integration required to calculate Φ accurately then had to be increased.

The tractions acting on the external surface of the specimen in its current state are given by $T_i^{(t)} = \hat{T}_i^{(t)} + \tilde{T}_i^{(t)}$ and the stored energy Φ_e associated with the applied loads is identified with the stored energy in a dislocation-free specimen having these tractions applied on its external surface. The stress and strain fields in this dislocation-free specimen are denoted by $\breve{\sigma}_{ij}$ and $\breve{\varepsilon}_{ij}$, respectively. These fields are determined by solving the linear elastic boundary value problem (using the finite element method) with tractions $T_i^{(t)}$ specified on the external surfaces of the crystal. The energy Φ_e at time t is then given by

$$\Phi_e = \frac{1}{2}\int_A \breve{\sigma}_{ij}\breve{\varepsilon}_{ij}\,\mathrm{d}A. \tag{9a}$$

Since the applied tractions $T_i^{(t)}$ need not result in a uniform stress field in the specimen, Φ_e is not necessarily equal to the energy

$$W_e = \frac{\sigma^2(1-\nu^2)}{2E}\,A, \tag{9b}$$

associated with a uniform stress σ. The corresponding energy Φ_d stored in the dislocation structure is then taken to be

$$\Phi_d = \Phi - \Phi_e. \tag{9c}$$

The total work Π done in straining the specimen to U^*/L is

$$\Pi = A\int_0^{U^*/L} \sigma\,\mathrm{d}(U/L), \tag{10}$$

with the plastic dissipation equal to $\Pi - \Phi$.

The normalized energies Φ_d/Π and Φ/Π at $U/L = 0.05$ are plotted in Figs. 5a and b, respectively as a function of the specimen size W (for both the calculations with rotation of the tensile axis unconstrained and constrained). With rotation of the

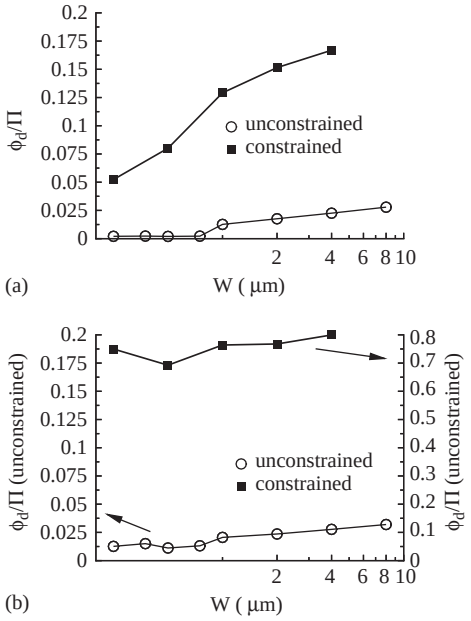

Fig. 5. Small-strain results for (a) the energy Φ_d stored in the dislocation structure and (b) total elastic energy Φ at an applied strain $U/L = 0.05$. The energies Φ_d and Φ are normalized by the total work done Π up to $U/L = 0.05$.

tensile axis unconstrained and for $W \leqslant 0.75\,\mu m$, negligible energy is stored in the dislocation structure with the elastic energy associated with the applied loads being the major contribution to Φ. On the other hand, for the larger specimens ($W > 1.0\,\mu m$), most of the stored energy is associated with the dislocation structure. However, in all cases with unconstrained rotation of the tensile axis, the stored energy is only about 2.5% of the total work done, the remaining energy being dissipated in plastic work. Since dislocation structures associated with geometrically necessary dislocations (GNDs) would give rise to a long range stress field which, in turn, would be accompanied by increased values of the stored elastic energy, the low values of Φ_d when the rotation of the tensile axis is unconstrained, are consistent with this size dependence not being related to GNDs.

3.1.1. Effects of dislocation sources and obstacles

The tensile stress–strain responses for three obstacle-free specimens are plotted in Fig. 6a and the evolution of the dislocation density ρ_{dis} with strain for the $W = 1.0$ and $8.0\,\mu m$ obstacle-free specimens is plotted in Fig. 6b. The specimens in Fig. 6 are identical to the reference specimens considered in Section 3.1 except that all obstacles have been removed. The stress–strain response of the $W = 0.25\,\mu m$ obstacle-free specimen is very similar to that of the reference material. However, the $W = 1.0$ and $8.0\,\mu m$ obstacle-free specimens have a much higher flow strength than the

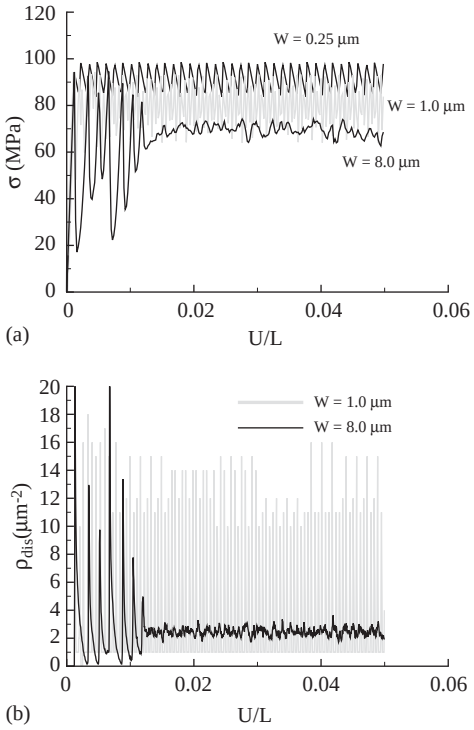

Fig. 6. Small-strain results for (a) the tensile response and (b) evolution of dislocation density with strain for crystals with no obstacles (rotation of the tensile axis unconstrained). Results in (a) are shown for three selected specimen sizes but only the $W = 1.0$ and $8.0\,\mu m$ results are included in (b) for the sake of clarity.

corresponding reference specimens. The very large oscillations in the applied stress and ρ_{dis} in the early stages of the response of the $W = 8.0\,\mu m$ specimen are a result of sudden bursts of dislocation nucleation. Since there are no obstacles to dislocation motion, the glide of these dislocations results in a drop in the applied stress. When these dislocations exit the specimen, the stress has to increase to approximately $2\bar{\tau}_{nuc}/\sin 2\phi$ to nucleate new dislocations for plastic deformation to continue. However, in this large specimen, the rate of dislocation nucleation is greater than the rate at which dislocations exit the specimen and thus eventually a steady-state is reached where a few dislocations remain within the specimen: the stress concentration associated with these dislocations enables continued nucleation of new dislocations at an applied stress below $2\bar{\tau}_{nuc}/\sin 2\phi$. On the other hand, dislocations continually nucleate and exit the $W = 1.0\,\mu m$ specimen with nearly no dislocation storage, as evidenced by the large oscillations in the stress–strain and ρ_{dis} versus U/L curves in Fig. 6. Thus,a stress approximately equal to $2\bar{\tau}_{nuc}/\sin 2\phi$ needs to be applied to ensure continued plastic deformation. When no obstacles are present in the specimen, $\rho_f \approx 2\,\mu m^{-2}$ for all specimen sizes, Fig. 6b. In contrast, ρ_f increases from approximately $2\,\mu m^{-2}$ to about $100\,\mu m^{-2}$ as the specimen size increases from

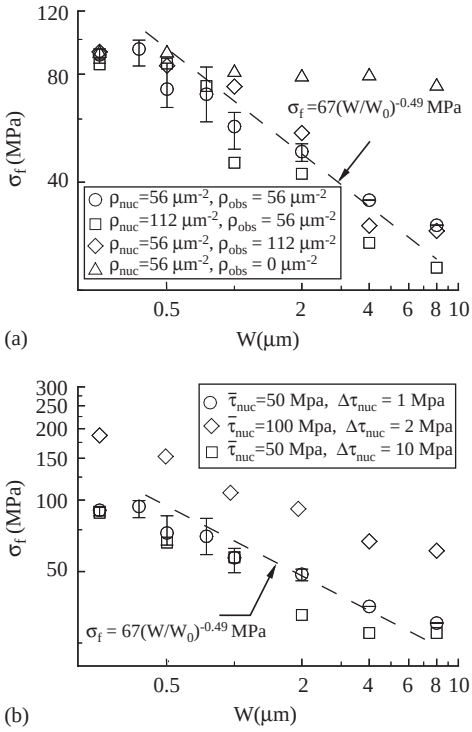

Fig. 7. Small-strain results (rotation of the tensile axis unconstrained) for the variation of the flow strength σ_f with specimen size W. Effect of (a) source and obstacle density and (b) mean source strength $\bar{\tau}_{nuc}$ and standard deviation $\Delta\tau_{nuc}$ of the source strengths.

$W = 0.25$ to $8.0\,\mu m$ in the reference specimens, Fig. 3b. It is this increase in dislocation density that results in the decrease in σ_f with increasing W.

The effect of obstacle density on the flow strength σ_f is illustrated in Fig. 7a. While σ_f displays a weak dependence on specimen size W in the obstacle-free crystals, doubling the reference obstacle density to $\rho_{obs} = 112\,\mu m^{-2}$ has a negligible effect on σ_f to within the statistical variations in the results. This indicates that a critical obstacle density is required to inhibit dislocation motion and facilitate storage of dislocations in the specimens. Below this critical density, the mean spacing between obstacles, $1/\sqrt{\rho_{obs}}$, is large compared to the specimen size and dislocations exit the specimen before being blocked by the obstacles. Above this critical density, over the range of obstacle densities considered, the obstacle density does not significantly affect the flow strength. The effect of source density on σ_f is also included in Fig. 7a. Increasing the source density from the reference value $\rho_{nuc} = 56$ to $112\,\mu m^{-2}$ reduces the flow strength for the $W \geqslant 1.0\,\mu m$ specimens but has a negligible effect on the flow strength of the smaller specimens.

The effect of increasing the source and obstacle strength to $\bar{\tau}_{nuc} = 100\,MPa$ and $\tau_{obs} = 300\,MPa$ on σ_f is illustrated in Fig. 7b. In these calculations, the same spatial

distribution of sources and obstacles as in the reference material was taken and the strength of each of source and obstacle increased by a factor of two. Thus, the corresponding standard deviation $\Delta\tau_{nuc}$ of source strengths also increased to 2 MPa. Increasing the source and obstacle strength by a factor of two increases the flow strength σ_f by a similar amount over the whole range of specimen sizes investigated here. The effect of increasing the standard deviation $\Delta\tau_{nuc}$ of the source strengths from 1 to 10 MPa, while keeping the source and obstacle densities as well as $\bar{\tau}_{nuc}$ and τ_{obs} fixed at the reference values, is also illustrated in Fig. 7b. The main effect of increasing the standard deviation of nucleation strengths is to decrease the size effect for sufficiently large W; that is, the lower plateau in $\sigma_f(W)$ occurs at a smaller value of W.

3.2. Tensile axis rotation constrained

The stress σ versus strain U/L curves of three sizes of the reference specimen subjected to uniaxial tension with the rotation of the tensile axis constrained are shown in Fig. 8a. As in the calculations with rotation of the tensile axis

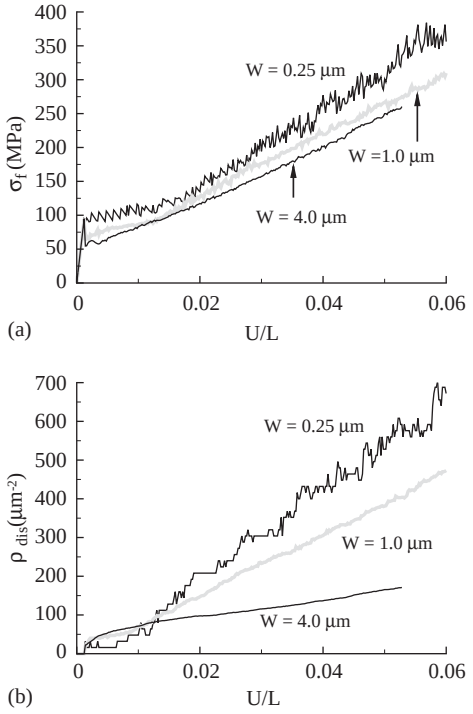

Fig. 8. Small-strain results for the tensile response (rotation of the tensile axis constrained) for specimens with $W = 0.25$, 1.0 and 4.0 μm. (a) Nominal stress versus nominal tensile strain and (b) evolution of the dislocation density with nominal tensile strain.

unconstrained, the first dislocation activity occurs at $\sigma \approx 95\,\text{MPa}$. Subsequently, the $W = 0.25\,\mu\text{m}$ specimen exhibits ideally plastic behavior up to $U/L = 0.015$ followed by a linear hardening response with a hardening rate $\mathrm{d}\sigma/\mathrm{d}(U/L) \approx G/6$, where G is the shear modulus. On the other hand, after the first dislocation nucleation, there is a sharp stress drop in the two larger specimens ($W = 1.0$ and $4.0\,\mu\text{m}$) and subsequently these specimens also exhibit similar linear hardening behavior. The corresponding evolution of the dislocation density ρ_{dis} (number of dislocations per unit area in a central $2L/3 \times W$ region) is shown in Fig. 8b. In contrast to the calculations with rotation of the tensile axis unconstrained, ρ_{dis} continues to increase approximately linearly with increasing U/L up to the strain levels computed here. Moreover, the rate $\mathrm{d}\rho_{\text{dis}}/\mathrm{d}(U/L)$ increases with decreasing W resulting in higher dislocation densities in the smaller specimens.

These results are summarized in Fig. 9 where the flow strength σ_{f} and corresponding dislocation density ρ_{f} (both averaged between $0.04 \leqslant U/L \leqslant 0.05$) are plotted in Figs. 9a and b, respectively, along with the data from Fig. 3 where rotation of the tensile axis is unconstrained. The power-law relation equation (6) is seen to fit the flow strength data for the calculations with rotation of the tensile axis constrained with $\alpha = 244\,\text{MPa}$ and $n = 0.08$. Thus, while the flow strength is much

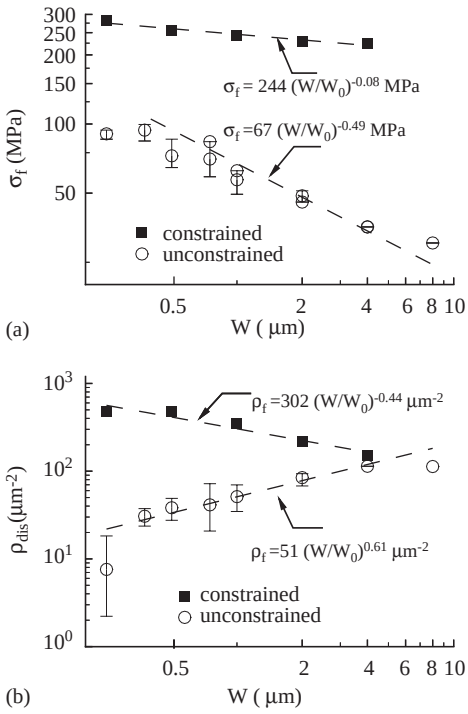

Fig. 9. Small-strain results for the variation of the (a) flow strength σ_{f} and (b) average dislocation density ρ_{f} with specimen size W for both the tensile axis rotation constrained and unconstrained boundary conditions.

higher when rotation of the tensile axis is constrained, the size dependence of the flow strength is significantly reduced compared to when rotation of the tensile axis is unconstrained. The dislocation densities ρ_f are also higher in the calculations with rotation of the tensile axis constrained, but ρ_f increases with decreasing size: Eq. (7) with $\beta = 302\,\mu m^{-2}$ and $m = -0.44$ describes the dependence of ρ_f on W.

The distribution of σ_{11} in the $W = 0.5, 2.0$ and $4.0\,\mu m$ specimens along with the corresponding dislocation structures at $U/L = 0.05$ are plotted in Figs. 10a–c, respectively. In all cases, the constraint imposed by restraining the tensile axis to remain parallel to the x_1 axis results in the development of bending stresses (the localized high stress regions seen around the points $(x_\varepsilon, 0)$ and $(2L - x_\varepsilon, 0)$ are associated with the constraint imposed by the supports at those locations). Also, distributions of lattice rotations (not shown here) indicate a band of concentrated lattice rotations at $\approx -45^\circ$ with respect to the x_1 axis. Consistent with the results in Deshpande et al. (2005) and the dislocation distributions in Fig. 10, this is a kink-like band perpendicular to the slip direction. While the arrangement of the dislocations in a kink-like band suggests that a large fraction of the dislocations may be viewed as "geometrically-necessary" in the sense of Ashby (1970), the scaling of ρ_f with W is not consistent with this assumption. The GND density ρ_G is expected to scale with W^{-1} while the discrete dislocation calculations suggest that $\rho_f \propto W^{-0.44}$. However,

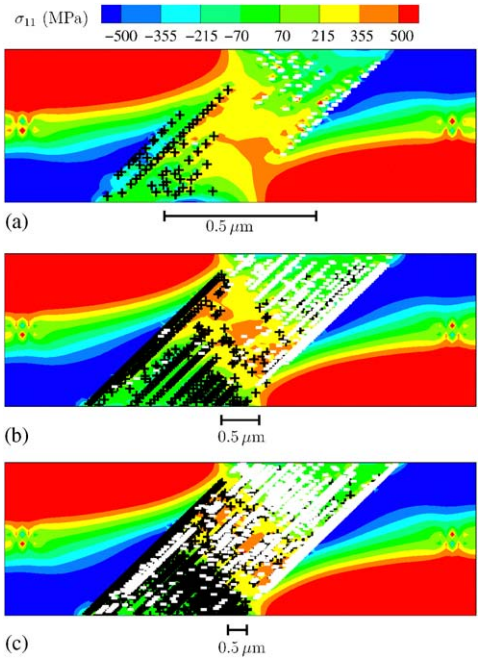

Fig. 10. Small-strain results (rotation of the tensile axis constrained) for the distribution of σ_{11} and the dislocation structure in the (a) $W = 0.5\,\mu m$, (b) $W = 2.0\,\mu m$ and (c) $W = 4.0\,\mu m$ specimens at an applied strain $U/L = 0.05$. The black "+" symbols denote dislocations with Burgers vector $+b$ and the white "−" symbols denote dislocations with Burgers vector $-b$ (see Fig. 1 for the sign convention).

with rotation of the tensile axis constrained, the specimen is subject to combined bending and tension and thus expected to have a substantial fraction of statistically stored dislocations in addition to GNDs. The density of statistically stored dislocations does not scale with the specimen size W which results in the weaker dependence of ρ_f on W in the calculations here.

The variations of the normalized energies Φ_d/Π and Φ/Π at $U/L = 0.05$ with specimen size W are included in Figs. 5a and b, respectively, along with the corresponding data from the calculations with rotation of the tensile axis unconstrained. A larger fraction of the total work done is stored in the dislocation structure when rotation of the tensile axis is constrained, with Φ_d/Π increasing from about 5% in the $W = 0.25\,\mu m$ specimen to about 18% when $W = 4.0\,\mu m$. Moreover, most of the work done is stored as elastic energy with Φ/Π nearly independent of W and approximately equal to 0.8. When rotation of the tensile axis is constrained, the elastic energy associated with the applied loads is expected to be much greater than that associated with a uniform applied tensile field. To illustrate this, the ratios Φ_e/W_e at $U/L = 0.05$ are plotted in Fig. 11 as a function of W for calculations both with rotation of the tensile axis unconstrained and constrained. With rotation of the tensile axis unconstrained, $\Phi_e \approx W_e$ suggesting that the applied loading is reasonably uniform. On the other hand, the imposed bending (Fig. 10) results in $\Phi_e/W_e \approx 10$ when rotation of the tensile axis is constrained. This imposed bending also gives rise to the hardening response of the specimens and the formation of the kink-like band visible in Fig. 10.

3.3. The Bauschinger effect

Since a large fraction of the total work is stored as elastic energy in the specimens with rotation of the tensile axis constrained, we expect such specimens to exhibit a strong Bauschinger effect (reverse plastic flow during unloading). In order to investigate this phenomenon, the $W = 0.25, 1.0$ and $4.0\,\mu m$ specimens were unloaded from $U/L = 0.05$ by applying a reverse strain rate $\dot{U}/L = -2000\,s^{-1}$ until $U/L = 0$.

The loading–unloading stress versus strain curves for calculations with the rotation of the tensile axis unconstrained and constrained, are plotted in Figs. 12a

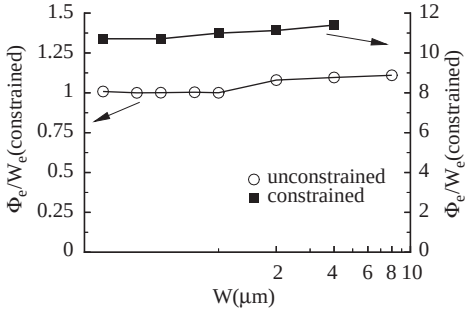

Fig. 11. Small-strain results for the ratio of the stored elastic energy Φ_e to the elastic energy W_e associated with a uniform tensile field at $U/L = 0.05$. Results from calculations with rotation of the tensile axis unconstrained and constrained conditions are included.

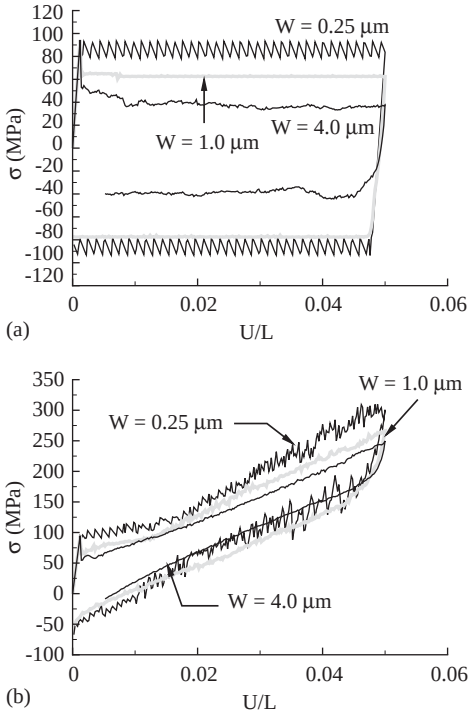

Fig. 12. Small-strain results for the loading–unloading response of the reference crystals with (a) rotation of the tensile axis unconstrained and (b) rotation of the tensile axis constrained.

and b, respectively. When rotation of the tensile axis is unconstrained, nearly no Bauschinger effect is observed with compressive yield occurring at a stress level approximately equal to the original tensile flow strength. This is consistent with the low values of elastic energy stored in the dislocation structure, seen in Figs. 5 and 11. This is also in good agreement with the experimental measurements of Dimiduk et al. (2005) on pure Ni. On the other hand, unloading with rotation of the tensile constrained results in reverse plastic flow with reverse yielding commencing at $\sigma \approx 150\,\mathrm{MPa}$. Subsequently, unloading occurs with the stress decreasing approximately linearly with strain with a slope equal to that during the initial loading; that is, $\mathrm{d}\sigma/\mathrm{d}(U/L) \approx G/6$ during reverse plastic flow.

4. Finite-strain effects

4.1. Finite-strain formulation

The results presented in Section 3 were obtained using a small-strain framework, i.e. neglecting changes in geometry of the specimen due to deformation. In order to

assess the consequences of this approximation on the phenomena investigated here, we also study the problem using the finite-strain dislocation plasticity framework of Deshpande et al. (2003). This framework assumes that (i) lattice strains remain small away from the dislocation cores and (ii) the elastic properties are unaffected by slip. In contrast to the small-strain calculations, the finite-strain framework accounts for: (i) finite deformation-induced lattice rotations and (ii) the effect of shape changes due to slip on the momentum balance.

As in the small-strain formulation, the total displacement rate and stress fields are given by a superposition of the analytically known ($\tilde{}$) fields of dislocations in an infinite medium and the ($\hat{}$) fields that enforce the boundary conditions. In contrast to the small-strain analysis, the complimentary problem for the ($\hat{}$) fields is nonlinear and is solved iteratively using an updated Lagrangian scheme. Readers are referred to Deshpande et al. (2003) for further details.

We summarize the plane strain short-range constitutive rules, highlighting the differences between the small-strain and finite-strain formulations. One significant change is that dislocations are no longer confined to a fixed slip plane due to slip on intersecting slip systems. Hence, the basic entity is a slip system (i.e. the orientation of the slip plane normal and the slip direction) rather than a slip plane. Furthermore, because of finite rotations, the orientation of a nucleated dislocation dipole (the two-dimensional analog of a nucleated loop) varies with the local deformation state.

The magnitude of the glide velocity $V_{\text{gln}}^{(I)}$ along the current slip direction $s_i^{*(\alpha)}$ of dislocation I on slip system α is again taken to be linearly related to the Peach–Koehler force $f^{(I)}$ through the drag relation $V_{\text{gln}}^{(I)} = f^{(I)}/B$. Here, we assume that the drag coefficient B is constant throughout the body. We also do not account for any change in the resistance to dislocation motion near a free surface associated with the energy required to create new free surface when the dislocation exits. Frank–Read sources generate a dislocation dipole with their Burgers vectors aligned with the local slip direction $s_i^{*(\alpha)}$. Note that unlike the small-strain formulation where only opposite signed dislocations on a given slip plane can annihilate each other, in the finite-strain context opposite signed dislocations on a given slip system can annihilate each other. Thus, annihilation of two opposite signed dislocations on a particular slip system occurs when they are within L_e irrespective of their current slip planes. Obstacles to dislocation motion are modeled as points associated with a slip system rather than a slip plane. Thus, dislocations on the obstacle slip system that pass within a specified distance, taken to be L_e, get pinned to that obstacle.

As in the small-strain calculations, in the finite-strain calculations, 80×40 quadrilaterals were employed in the finite element discretization of all the specimens. However, in this case, each quadrilateral was built-up of four triangular elements with linear displacement fields. The finite-strain calculations are limited by the distortion of the finite element mesh because deformation can be highly localized. In order to increase the strain levels that can be attained, without substantially affecting the accuracy of the calculations, a simple re-meshing scheme was employed as discussed in the Appendix.

4.2. Boundary conditions and crystal properties

In the finite-strain context, and with the tensile axis aligned with the x_1 direction, tension or compression is imposed by prescribing the displacement rates $\dot{u}_i$ and traction rates $\dot{T}_i$ as

$$\dot{u}_1 = \dot{U}, \quad \dot{T}_2 = 0 \quad \text{on } x_1 = 2L + U, \tag{11a}$$

and

$$\dot{u}_1 = -\dot{U}, \quad \dot{T}_2 = 0 \quad \text{on } x_1 = -U. \tag{11b}$$

The lateral edges, those initially on $x_2 = \pm W/2$, are traction free, i.e.

$$\dot{T}_1 = \dot{T}_2 = 0. \tag{12}$$

As in the small-strain calculations, the specimens are subjected to a nominal loading rate $|\dot{U}|/L = 2000\,\mathrm{s}^{-1}$. With these common set of boundary conditions, we again explore the effect of the constraint imposed by the tensile grips by considering rotation of the tensile axis as being constrained or unconstrained. These conditions are

(i) *Unconstrained rotation of the tensile axis*: $\dot{u}_2 = 0$ is imposed on one material point at $(2L - x_\varepsilon, 0)$ in the undeformed configuration, where $x_\varepsilon = 0.1L$.
(ii) *Constrained rotation of the tensile axis*: $\dot{u}_2 = 0$ is imposed on two material points at $(x_\varepsilon, 0)$ and $(2L - x_\varepsilon, 0)$ in the undeformed configuration, where $x_\varepsilon = 0.1L$.

4.3. Finite-strain numerical results

The finite-strain discrete dislocation plasticity calculations indicate a tension–compression asymmetry. Therefore the responses in tension and compression are discussed separately in this section.

4.3.1. Tensile axis rotation unconstrained

The nominal stress, σ_{nom}, versus strain, U/L, responses of three selected specimens subjected to uniaxial tension and compression are plotted in Figs. 13a and b, respectively. The stress, σ_{nom}, is computed as

$$\sigma_{\mathrm{nom}}(t) = -\frac{1}{W}\int_{S_L} T_1 \,\mathrm{d}s. \tag{13}$$

Here, the integration is performed along the boundary S_L where $x_1 = -U$. A comparison with Fig. 2a reveals that the small- and finite-strain predictions of the tensile responses of the $W = 4.0\,\mu\mathrm{m}$ specimen are reasonably similar, with both calculations predicting an almost ideally plastic response for $U/L > 0.02$. On the other hand, the finite-strain calculations predict a hardening tensile response for the $W = 2.0$ and $0.5\,\mu\mathrm{m}$ specimens with $\mathrm{d}\sigma_{\mathrm{nom}}/\mathrm{d}(U/L) \approx G/80$ and $G/30$, respectively.

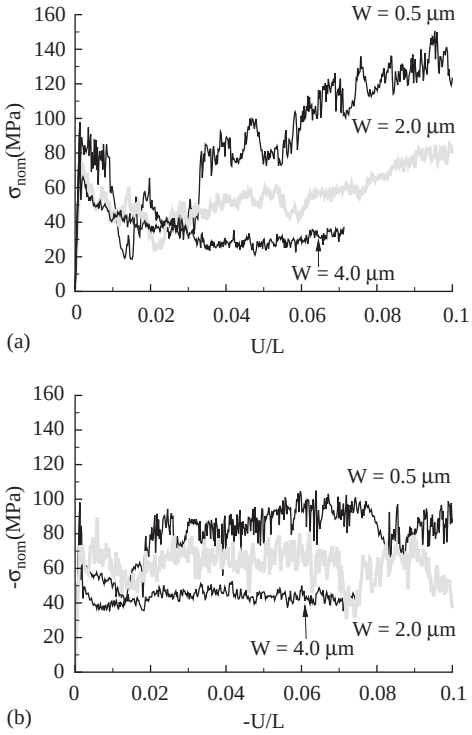

Fig. 13. Finite-strain results (rotation of the tensile axis unconstrained) for the (a) tensile and (b) compressive responses of specimens with $W = 0.25, 1.0$ and $4.0\,\mu m$.

The finite-strain compressive response, Fig. 13b, is almost ideally plastic for all specimen sizes considered.

The finite-strain and small-strain predictions of the flow strength σ_f for the reference specimens are plotted in Fig. 14a, as a function of the specimen size W. In line with the small-strain calculations, σ_f in these finite-strain calculations is defined as the absolute value of the average nominal stress between $0.04 \leqslant |U|/L \leqslant 0.05$. For specimen sizes in the range $0.5\,\mu m \leqslant W \leqslant 4.0\,\mu m$, the finite-strain tension calculations predict that σ_f increases with decreasing W, following a scaling law similar to the small-strain predictions, Eq. (6). The finite-strain results for the dislocation densities ρ_f (number of dislocations per unit area in a central $2L/3 \times W$ region averaged between $0.04 \leqslant |U|/L \leqslant 0.05$) are shown in Fig. 14b, along with the small-strain results from Fig. 3b. Again, the finite-strain calculations predict a scaling[1] similar to the small-strain calculations.

[1]The $W = 1.0$ and $2.0\,\mu m$ finite-strain tension calculations predict dislocation densities higher than those in the corresponding finite-strain compression and small-strain calculations. Additional calculations are needed to establish whether this is indicative of a trend or a result of the statistical scatter inherent in the discrete dislocation predictions.

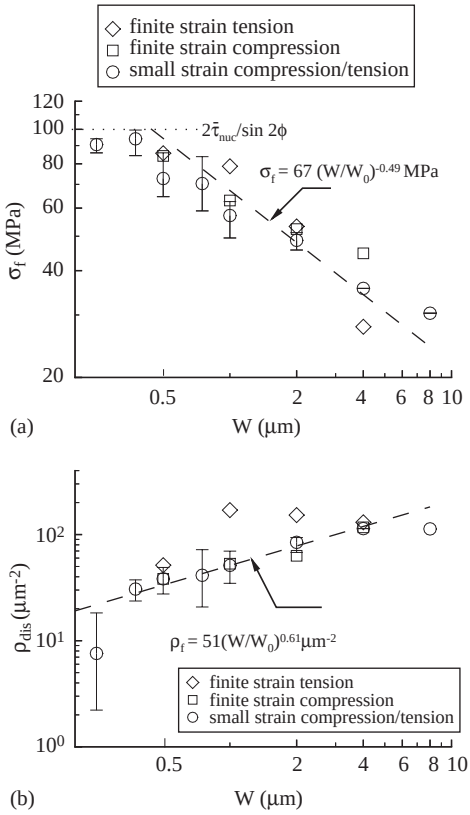

Fig. 14. Small- and finite-strain results for the variation of the (a) flow strength σ_f and (b) average dislocation density ρ_f with specimen size W for the tensile axis rotation unconstrained boundary condition.

To gain some insight into the differences between the finite-strain results for the tensile and compressive responses of the $W = 0.5\,\mu m$ specimen, the distribution of Cauchy stress σ_{11} at $|U|/L \approx 0.05$ are plotted in Figs. 15a and b for the uniaxial tension and compression cases, respectively. The corresponding dislocation structures are also included in Fig. 15. As in the small-strain predictions, the finite-strain calculations also indicate that very few dislocations are present in the specimen at $|U|/L \approx 0.05$. However, while the stress distribution is nearly uniform in the small-strain case, Fig. 4a, a large boundary layer with high stresses develops along the traction free edges in finite-strain, Fig. 15a. The hardening tensile response of the $W = 0.5\,\mu m$ specimen is due to the growth of the boundary layer with increasing strain. A thinner boundary layer develops in the finite-strain compression calculation, Fig. 15b, with the stress distribution more uniform. Finite-strain results for the Cauchy stress σ_{11} distribution and dislocation structure in the $W = 4.0\,\mu m$ tensile specimen are shown in Fig. 15c. As in the small-strain

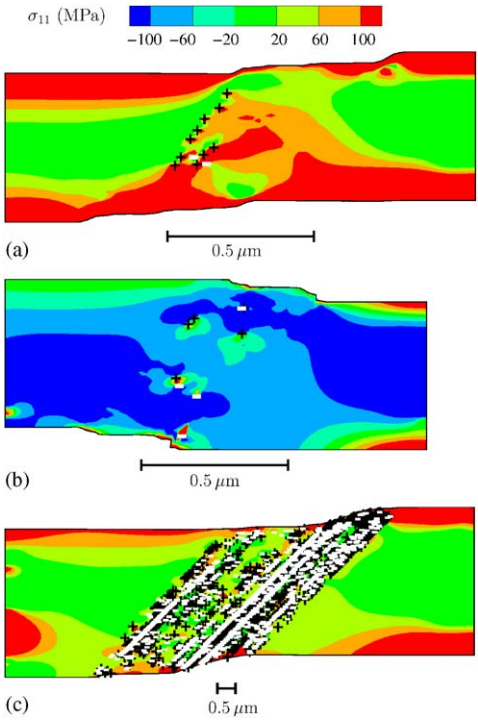

Fig. 15. Finite-strain results (rotation of the tensile axis unconstrained) for the distribution of the Cauchy stress component σ_{11} and the dislocation structure at an applied strain $|U|/L \approx 0.05$. (a) Tension and (b) compression of the $W = 0.5\,\mu$m specimen and (c) uniaxial tension of the $W = 4.0\,\mu$m specimen. The black "+" symbols denote dislocations with Burgers vector $+b$ and the white "−" symbols denote dislocations with Burgers vector $-b$ (see Fig. 1 for the sign convention).

calculations, the stress distribution is more uniform in the $W = 4.0\,\mu$m specimen than in the smaller specimens, although there still is a small boundary layer. The boundary layer occurs because the kinematic boundary conditions equation (11) prevent rotation of the ends of the specimens, even though the tensile axis can rotate.

4.3.2. Tensile axis rotation constrained

The finite-strain tension and compression responses when rotation of the tensile axis is constrained are shown in Figs. 16a and b, respectively. In tension, hardening is linear with $\mathrm{d}\sigma_{\mathrm{nom}}/\mathrm{d}(U/L) \approx G/15$ for specimen sizes from $W = 0.5$ to $4.0\,\mu$m. This hardening rate is about a factor of two smaller than that in the small-strain analyses, Fig. 8a. However, under uniaxial compression, the finite-strain calculations predict a linear hardening rate similar to that in the small-strain calculations.

The finite-strain predictions of the variations of the flow strength σ_{f} and dislocation density ρ_{f} with W are summarized in Figs. 17a and b, respectively, along

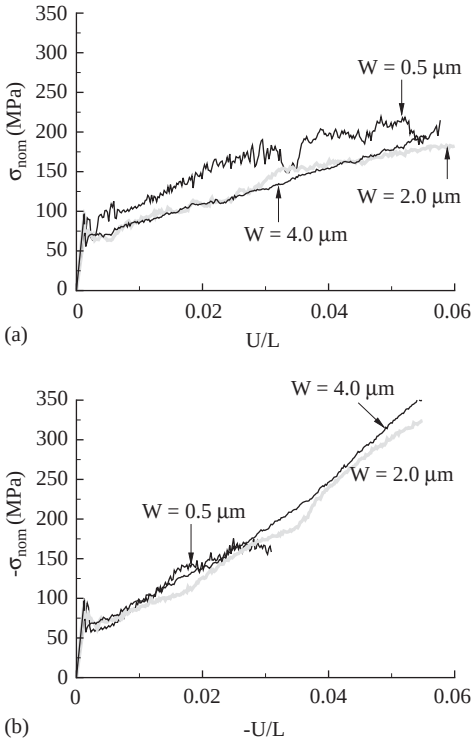

Fig. 16. Finite-strain results (rotation of the tensile axis constrained) for the (a) tensile and (b) compressive responses of specimens with $W = 0.5, 2.0$ and $4.0\,\mu m$.

with the appropriate small-strain predictions.[2] In tension, with rotation of the tensile axis constrained, the finite-strain calculations predict a scaling of σ_f with W similar to the small-strain calculations, albeit with a slightly reduced flow strength. On the other hand, in compression with rotation of the tensile axis constrained, the finite-strain calculations predict that σ_f increases slightly with increasing W though there is insufficient finite-strain data to make a conclusive statement. The finite-strain predictions of ρ_f are very similar to the small-strain predictions over the specimen size range $0.5\,\mu m \leqslant W \leqslant 4.0\,\mu m$.

Figs. 18a and b depict the distributions of the Cauchy stress σ_{11} and the dislocation structures in the $W = 4.0\,\mu m$ specimen at $|U|/L \approx 0.05$ for tension and compression, respectively. As in the small–strain calculations, the finite-strain analysis predicts that the constraint imposed by restraining the rotation of the tensile axis results in the formation of a kink-like band at $\approx -45^\circ$ with respect to the x_1 axis

[2]The $W = 0.5\,\mu m$ compression calculations were terminated at $U/L \approx 0.03$ as excessive surface roughening meant that the simple re-meshing technique was no longer able to effectively re-mesh the domain. Thus, the finite-strain compression data for this case is not included in Fig. 17.

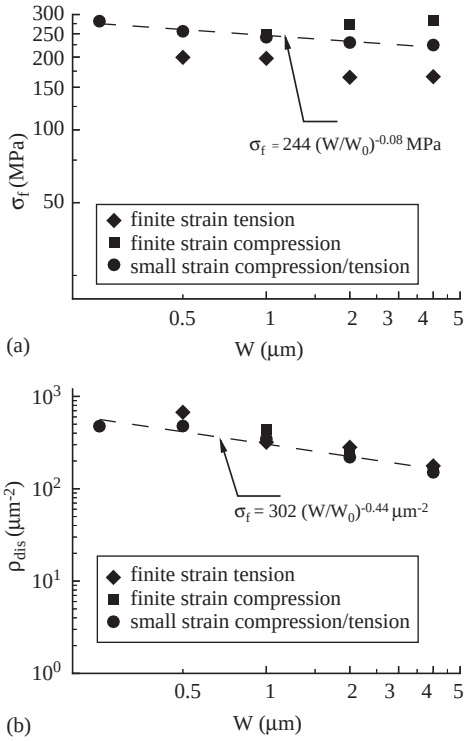

Fig. 17. Small-strain and finite-strain results for the variation of the (a) flow strength σ_f and (b) average dislocation density ρ_f with specimen size W for the tensile axis rotation constrained boundary condition.

(i.e. perpendicular to the original slip direction) and in the development of large bending stresses. These large bending stresses (which are also seen in the small-strain analyses) result in the development of lattice rotation and suggest the need for the finite-strain framework.

5. Discussion

With the tensile axis constrained against rotation, the flow strength and dislocation density decrease with increasing specimen size. While the size dependence of the flow strength is weak ($\sigma_f \propto W^{-0.08}$), the dislocation density scales with $W^{-0.44}$. The decreasing dislocation density with increasing specimen size is consistent with the role of bending when rotation of the tensile axis is constrained, as the density of geometrically necessary dislocations is proportional to 1/specimen size (Nye, 1953; Ashby, 1970). The combined tension and bending in cases where the tensile axis is constrained leads to the reduced dependence of the dislocation density on W.

On the other hand, when rotation of the tensile axis is permitted, there is a size regime where the flow strength decreases strongly with increasing specimen size,

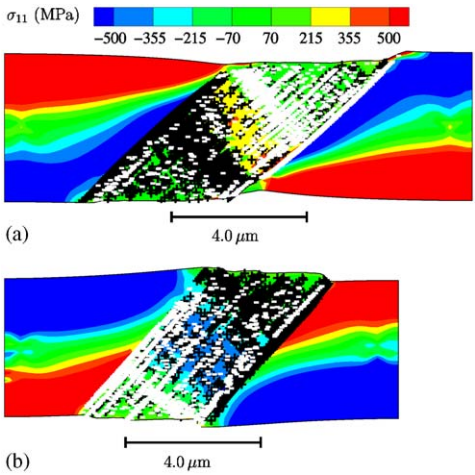

Fig. 18. Finite-strain results (rotation of the tensile axis constrained) for the distribution of the Cauchy stress component σ_{11} and the dislocation structure in the $W = 4.0\,\mu m$ specimen at an applied strain $|U|/L \approx 0.05$. (a) Tension and (b) compression. The black "+" symbols denote dislocations with Burgers vector $+b$ and the white "−" symbols denote dislocations with Burgers vector $-b$ (see Fig. 1 for the sign convention).

approximately $\propto W^{-0.5}$, and the dislocation density at a given strain increases with increasing specimen size. The origin of this size effect is quite different from when rotation of the tensile axis is constrained. Because the calculations begin with the specimen free of mobile dislocations, plastic deformation begins when the resolved shear stress at the weakest dislocation source attains the nucleation strength for the required nucleation time. Thus, one contribution to the size effect is that, since the source density is taken to be independent of specimen size, larger specimens have more dislocation sources than small specimens and are more likely to have a weak source. But this is not the main contribution to the size dependence as the standard deviation of the source strengths in most calculations is just 1 MPa. The main contribution is associated with the role of the dislocation obstacles in preventing dislocations from exiting the specimen. Since the density of dislocation obstacles is the same for all specimen sizes, the mean distance between obstacles is independent of specimen size. Therefore, for a sufficiently small specimen, the distance a dislocation needs to glide to exit the specimen is less than the mean distance between obstacles and dislocations are likely to leave the specimen without encountering an obstacle. Continued plastic deformation thus requires the stress to be maintained at the nucleation strength. For larger specimens, dislocation glide is more likely to be blocked by obstacles. The stress concentration associated with the elastic fields of the dislocations enables the activation of dislocation sources when the applied stress is less than the nucleation strength. Hence, the flow strength decreases and the dislocation density increases with increasing specimen size. In our calculations, it is the stress concentration associated with an increased number of internal dislocations

that promotes plastic flow at a lower applied stress in larger specimens. Also, our calculations suggest that the key ratios for the size dependence are that of specimen size to obstacle spacing, and specimen size to source spacing.

Consistent with this picture, Fig. 2a shows that the initial yield strength for the $W = 4.0\,\mu m$ specimen is nearly the same as that for the $W = 0.25\,\mu m$ specimen. It is only after some plastic deformation and when an internal dislocation density has developed that the lower flow strength of the larger specimen is attained. On the other hand, the dislocation density in the obstacle-free crystals is about an order of magnitude smaller than the corresponding reference specimens. This results in the reduced size dependence of σ_f in the obstacle-free crystals (Fig. 7). Nevertheless, for the larger specimens, some dislocations do remain in the interior of the obstacle-free specimens simply because of the time it takes for the dislocation to traverse the slip plane. This suggests that for a relatively obstacle-free specimen, the number of internal dislocations may strongly depend on the imposed strain rate and the time t_{nuc} for the generation of a stable dislocation dipole.

Our analyses indicate that the main features of the size dependence emerge from a small-strain analysis. However, finite deformation effects (e.g. lattice rotations and shape changes) affect the predicted hardening rate and give rise to a tension–compression asymmetry. In the finite-strain analysis with rotation of the tension axis permitted, a boundary layer of high stress is found in the smaller specimens (Fig. 15a) although such a boundary layer is not seen in the corresponding small-strain analysis (Fig. 4a). However, the stress elevation in the boundary region in Fig. 15 is much less than when the rotation of the tensile axis is constrained, Figs. 10 and 18. It is worth noting that in Figs. 10 and 18, the size of the high stress region scales with the specimen size in contrast, for example, to thin films on substrates (Nicola et al., 2003). For thin films, a boundary layer develops as a consequence of impenetrability of the film–substrate interface, and has a thickness which is more or less independent of film thickness. The scaling of the high stress region here undoubtedly plays a role in the weak size dependence that occurs when the rotation of the tensile axis is constrained.

The qualitative features of the size dependence that emerge from our calculations are in good agreement with those seen in the experiments of Greer et al. (2005) for gold (where the size dependence of flow strength in the micron range goes as a -0.5 power) and by Dimiduk et al. (2005) for nickel (where the size dependence follows a -0.62 power law). For Ni_3Al intermetallics, Dimiduk et al. (2005) obtain a size dependence power of -0.77. The relatively high Peierls stress of intermetallics may play a role in the increased sensitivity to size. The ratio of the small to large specimen flow strengths in our calculations is about 3–5 whereas in the experiments a ratio of 5–10 is more typical.

Another significant difference between our calculations and the experiments of Uchic et al. (2004), Greer et al. (2005) and Dimiduk et al. (2005) is that the experimental measurements do not exhibit initial stress drops. The main factors that lead to this discrepancy are: (i) the experiments are essentially stress controlled while in the calculations a constant nominal strain rate was imposed; (ii) the strengths of all the dislocation sources were taken to be approximately equal; and (iii) our

analyses presume an initially stress-free specimen, whereas in a real specimen there is an initial dislocation structure. The associated initial stress field can have a significant effect on the stress–strain response at small strains. In our calculations, the applied stress must attain the nucleation stress of the weakest source for plastic flow to occur. Therefore, for the larger specimens there is a stress drop from the stress at initial yield to the stress for sustained plastic flow which can be reduced (or eliminated) by incorporating an initial dislocation distribution. Indeed, as seen in Fig. 12a, the stress drop is eliminated on reverse loading with the size dependence remaining unaffected. The stress drop is also reduced when there is a distribution of source strengths; this is seen in the stress–strain curves (not exhibited here) for the cases with $\Delta\tau_{\text{nuc}} = 10\,\text{MPa}$ in Fig. 7b.

Although the main features of size dependence agree with the cited experimental findings, our model contains a number of idealizations that may be responsible for the differences between our predictions and what is seen in the experiments. Our analyses are carried out within a two-dimensional plane strain framework. This significantly limits the sort of dislocation interactions that can occur. For example, the number of dislocation sources and obstacles are fixed whereas in a real specimen they are expected to evolve with deformation. The computational time required for a parameter study involving full three-dimensional analyses to the strains needed is not, at least for us, feasible at present. However, Benzerga et al. (2004) have recently developed dislocation constitutive rules to incorporate the physics of three-dimensional dislocation interactions into a two-dimensional computation.

In the current calculations, we have only permitted dislocation activity on a single slip system. When the crystals are oriented for symmetric double slip as in Greer et al. (2005), the results with rotation of the tensile axis constrained may differ significantly from those reported here. Even when dislocation activity on secondary systems contributes little to the overall plastic deformation as in Uchic et al. (2004), this secondary slip can influence the dislocation evolution on the primary system. The effect of multiple slip on size dependence in tension and compression can be investigated within the framework employed here.

The development of size-dependent phenomenological continuum plasticity constitutive relations for crystalline solids has focused on representing the role of plastic strain gradients and geometrically necessary dislocations. The results here show that discrete dislocation plasticity can represent size effects associated with the collective behavior of dislocations that, at least in certain circumstances, can give rise to size effects that are as strong as or stronger than those associated with geometrically necessary dislocations. Whether or not phenomenological plasticity relations can be developed that incorporate this source of size dependence remains to be seen.

6. Concluding remarks

We have carried out small- and finite-strain discrete dislocation analyses of the compressive and tensile responses of single crystals oriented for single slip under

plane strain conditions. The effect of the constraint imposed by the specimen grips is investigated by either constraining or permitting the rotation of the tensile axis of the crystals. Plastic flow arises from the collective motion of discrete dislocations that nucleate from initially present internal Frank–Read sources.

- When rotation of the tensile axis is constrained, bending is induced in the specimen in both the small- and finite-strain analyses with the build-up of geometrically necessary dislocations resulting in a linear hardening response and a weak size dependence of the flow strength σ_f but a strong Bauschinger effect. The dislocation density at a fixed applied strain decreases with increasing specimen size.
- When rotation of the tensile axis is unconstrained, a strong size effect is obtained with σ_f increasing with decreasing specimen size. However, there is a negligible Bauschinger effect and the dislocation density at a fixed applied strain increases with increasing specimen size.
- The main features of the size dependence are revealed by a small-strain analysis, although the finite-strain analyses suggest some tension–compression asymmetry.
- The mechanism for the increasing strength with decreasing size when rotation of the tensile axis is unconstrained is largely consistent with the "dislocation starvation" picture of Greer et al. (2005).

Acknowledgments

Support from the Materials Research Science and Engineering Center on *On Micro-and Nano-Mechanics of Electronic and Structural Materials* at Brown University (NSF Grant DMR-0079964) and the Leverhulme Trust, UK is gratefully acknowledged. The authors are pleased to acknowledge Dr. Dennis Dimiduk (Air Force Research Laboratory) for insightful comments and discussions during the course of this work.

Appendix: Details of the re-meshing scheme employed in the finite-strain calculations

A simple re-meshing scheme was employed in the finite-strain analysis so as to enable the calculations to proceed to larger deformations. In this re-meshing scheme, the number and type of elements along with the boundary nodes in the new and old mesh are kept fixed. Thus, the connectivity table of the elements remains unchanged and the re-meshing mainly comprises the transfer of the field quantities, such as stress, from the old mesh to the new mesh.

As in the original mesh, the new mesh is comprised of quadrilaterals built up of four triangular elements with linear displacement fields. The quadrilaterals are generated as follows. Let there be n and m nodes along the edges $x_2 = W/2$ and $x_1 = 0$ in the original mesh. The nodes along all the edges remain the same in the new and old mesh. Straight lines are drawn connecting each of the n nodes on the lateral

edge, initially on $x_2 = W/2$ to the corresponding node on the edge initially on $x_2 = -W/2$. Nodes of the quadrilateral elements in the new mesh are then generated by dividing each of these straight lines into $m-1$ equal segments.

It now remains to specify the values of the field quantities such as stress in the new mesh. Recall that we employ a mesh comprising quadrilaterals built up of four triangular elements with linear displacement fields. Thus, quantities such as stress and deformation gradient F_{ij} are constant within each triangular element. In order to estimate the stress σ_{ij} of a particular triangular element in the new mesh, we determine the position of the centroid of that triangular element. This point is then located in the old mesh and the new element assigned the stress value of the old triangular element in which this centroidal point lies. Re-meshing is carried out when

$$|\Delta \bar{F}| \geqslant (\Delta \bar{F}_{\max}), \tag{A.1a}$$

in any element. Here $\bar{F} = \sqrt{F_{ij}F_{ij}}$ where the deformation gradient,

$$F_{ij} = \delta_{ij} + \int_0^t \frac{\partial \dot{u}_i}{\partial x_m} F_{mj}^{-1}\, \mathrm{d}t. \tag{A.1b}$$

Spatial differentiation with respect to x_j is carried out using the finite element shape functions in the current configuration and thereby including the slip contribution. The Δ in (A.1a) denotes the change since the last re-meshing. The limiting value $(\Delta \bar{F})_{\max}$ was taken to be 0.6 in most of the calculations.

References

Ashby, M.F., 1970. The deformation of plastically non-homogeneous materials. Philos. Mag. 21, 399–424.

Benzerga, A.A., Bréchet, Y., Needleman, A., Van der Giessen, E., 2004. Incorporating three-dimensional mechanisms into two-dimensional dislocation dynamics. Modelling Simulation Mater. Sci. Eng. 12, 159–196.

De Guzman, M.S., Neubauer, G., Flinn, P., Nix, W.D., 1993. The role of indentation depth on the measured hardness of materials. Mater. Res. Soc. Symp. Proc. 308, 613–618.

Deshpande, V.S., Needleman, A., Van der Giessen, E., 2003. Finite strain discrete dislocation plasticity. J. Mech. Phys. Solids 51, 2057–2083.

Deshpande, V.S., Needleman, A., Van der Giessen, E., 2005. Discrete dislocation plasticity analysis of single slip tension. Mater. Sci. Eng. A 400–401, 154–157.

Dimiduk, D.M., Uchic, M.D., Parthasarathy, T.A., 2005. Size-affected single-slip behavior of pure nickel microcrystals. Acta Materialia 53, 4065–4077.

Ebeling, R., Ashby, M.F., 1966. Dispersion hardening of copper single crystals. Philos. Mag. 13, 805–834.

Fleck, N.A., Muller, G.M., Ashby, M.F., Hutchinson, J.W., 1994. Strain gradient plasticity: theory and experiment. Acta Metallurgica et Materialia 42, 475–487.

Greer, J.R., Oliver, W.C., Nix, W.D., 2005. Size dependence of mechanical properties of gold at the micron scale in the absence of strain gradients. Acta Materialia 53, 1821–1830.

Haque, M.A., Saif, M.T.A., 2004. Deformation mechanisms in free-standing nanoscale thin films: a quantitative in situ transmission electron microscope study. Proc. Nat. Acad. Sci. 101, 6335–6340.

Hughes, D.A., Hansen, N., 1993. Microstructural evolution in nickel during rolling from intermediate to large strains. Metall. Trans. A24, 2021–2037.

Kubin, L.P., Canova, G., Condat, M., Devincre, B., Pontikis, V., Bréchet, Y., 1992. Dislocation microstructures and plastic flow: a 3D simulation. Solid State Phenomena 23–24, 455–472.

Legros, M., Elliott, B.R., Rittner, M.N., Weertman, J.R., Hemker, K.J., 2000. Microsample tensile testing of nanocrystalline metals. Philos. Mag. A 80, 1017–1026.

Ma, Q., Clarke, D.R., 1995. Size dependent hardness of silver single crystals. J. Mater. Res. 10, 853–863.

Nicola, L., Van der Giessen, E., Needleman, A., 2003. Discrete dislocation analysis of size effects in thin films. J. Appl. Phys. 93, 5920–5928.

Nye, J.F., 1953. Some geometrical relations in dislocated crystals. Acta Metallurgica 1, 153–162.

Uchic, M.D., Dimiduk, D.M., Florando, J.N., Nix, W.D., 2004. Sample dimensions influence strength and crystal plasticity. Science 305, 986–989.

Van der Giessen, E., Needleman, A., 1995. Discrete dislocation plasticity: a simple planar model. Modelling Simulation Mater. Sci. Eng. 3, 689–735.

Xiang, Y., Vlassak, J.J., Perez-Prado, M.T., 2004. The effects of passivation layer and film thickness on the mechanical behavior of freestanding electroplated Cu thin films with constant microstucture. Mat. Res. Soc. Symp. Proc. 795, 417–422.

Zupan, M., Hayden, M.J., Boehlert, C.J., Hemker, K.J., 2001. Development of high temperature microsample testing. Exp. Mech. 41, 242–247.